A Novel High-Strength Zn-3Ag-0.5Mg Alloy Processed by Hot Extrusion, Cold Rolling, or High-Pressure Torsion

MARIA WĄTROBA, WIKTOR BEDNARCZYK, JAKUB KAWAŁKO,
SEBASTIAN LECH, KRZYSZTOF WIECZERZAK, TERENCE G. LANGDON,
and PIOTR BAŁA

A novel Zn-3Ag-0.5Mg alloy was plastically deformed using 3 processing paths: hot extrusion (HE), HE followed by cold rolling (CR) and high-pressure torsion (HPT). The processed samples consisted of the η-Zn phase, ε-Zn$_3$Ag precipitates within the matrix, and nanometric Zn$_2$Mg precipitates within the Zn$_{11}$Mg$_2$ phase located at the grain boundaries. Both the η-Zn phase and Mg-rich phases were enriched in Ag. Electron backscattered diffraction was used to examine the effects of grain size and texture on mechanical behavior with tensile tests performed at room temperature (RT) at different strain rates. The coarse-grained (~ 6 μm) samples after HE exhibited high strength with brittleness due to dislocation interaction with dispersed precipitates and, to some extent, with twinning activation. Significant grain refinement and processing at RT gave an increase in elongation to over 50 pct in CR and 120 pct in HPT. Ductile CR samples with an average grain size of ~ 2 μm and favorable rolling deformation texture gave a yield strength of ~ 254 MPa, a tensile strength of ~ 456 MPa, and a reasonable strain rate sensitivity. These values for the CR samples meet the mechanical requirements for biodegradable stents in cardiovascular applications.

MARIA WĄTROBA and WIKTOR BEDNARCZYK are with the Faculty of Metals Engineering and Industrial Computer Science, AGH University of Science and Technology, Al. A. Mickiewicza 30, 30-059 Krakow, Poland. Contact e-mail: mwatroba@agh.edu.pl JAKUB KAWAŁKO is with the Academic Centre for Materials and Nanotechnology, AGH University of Science and Technology, Al. A. Mickiewicza 30, 30-059 Krakow, Poland. SEBASTIAN LECH is with the Faculty of Metals Engineering and Industrial Computer Science, AGH University of Science and Technology and also with the International Centre of Electron Microscopy for Materials Science, AGH University of Science and Technology, Al. A. Mickiewicza 30, 30-059 Krakow, Poland. KRZYSZTOF WIECZERZAK is with the Laboratory for Mechanics of Materials and Nanostructures, Empa, Swiss Federal Laboratories for Materials Science and Technology, Feuerwerkerstrasse 39, 3602 Thun, Switzerland. TERENCE G. LANGDON is with the Department of Mechanical Engineering, Materials Research Group, University of Southampton, Southampton SO17 1BJ, UK. PIOTR BAŁA is with the Faculty of Metals Engineering and Industrial Computer Science, AGH University of Science and Technology and also with the Academic Centre for Materials and Nanotechnology, AGH University of Science and Technology.

I. INTRODUCTION

CONTINUOUS medical development and objectives for improving the quality of human lives have created high demands in the field of materials engineering, especially when designing new materials for load-bearing applications. In recent years, zinc and zinc alloys have gained increasing interest as metallic materials in the capacity of short-term biodegradable implants because of their optimal corrosion rate and biocompatibility. However, the use of pure Zn in the as-cast state for any structural application is not practical due to its inherent brittleness and poor mechanical properties.[1]

According to the requirements for cardiovascular applications,[2] the yield strength (YS), ultimate tensile strength (UTS), and elongation to failure (E_F) should exceed 200 MPa, 300 MPa, and ~18 pct, respectively. Furthermore, the minimum value for E_F should be in the range of 30 pct when considering the flexibility that is essential for the expansion of stents in blood vessels. The materials used for stents should exhibit a high UTS/YS ratio, sufficient ductility, and a high strain hardening rate in order to avoid localized strain concentrations. Additionally, there are other concerns, including the

high strain rate sensitivity (SRS) of Zn, the susceptibility to creep, and natural aging.[1] Also, time-dependent behavior under a constant load and/or very low strain rates and the possibility of secondary phase precipitation at room temperature (RT) may produce significant microstructural and mechanical properties changes leading to sudden localized damage of the stent.

The low melting temperature of Zn (T_m = 419.5 °C) contributes to its recrystallization temperature of approximately 12 °C.[3] Therefore, strengthening by plastic deformation is impossible as the deformed grains undergo rapid recovery as well as grain growth at RT. Another strengthening approach is via grain refinement which, as indicated by the Hall–Petch relationship, increases the yield strength and plasticity but only down to a critical grain size.[4–6] The effect of grain refinement strengthening was partially observed in hot extruded Zn-Zr,[7] Zn-Ag,[8] Zn-Cu,[9] Zn-Al, and Zn-Mg[10] alloys. However, in these alloys the mechanical properties may improve because of solid solution strengthening, the presence of second phase precipitates, crystallographic texture, and changing deformation modes which are also considered in the Hall–Petch equation.[11,12]

The low solubility of elements in Zn means that only a few may form solid solutions with Zn at RT and only at relatively small concentrations. These elements can contribute to grain size reduction and changes in the mechanisms taking place during deformation.[13] Nevertheless, solid solution strengthening alone is not sufficient to meet all of the mechanical requirements. Earlier research showed that excessive grain size reduction, below ~3 μm in quasi-single phase Zn alloys after equal-channel angular pressing (ECAP), leads to extreme elongations of more than 600 pct and a significant drop in mechanical strength compared to coarse-grained hot-extruded alloys.[14] In addition, the precipitation of secondary phases strengthens grain boundaries and successfully hinders the recrystallization-induced grain growth occurring during hot deformation.[7–9,15,16]

Thus, the fabrication of high-strength ductile Zn alloys with microstructural stability is challenging, but the approach has been addressed by designing binary and ternary alloys using different castings, additive manufacturing, and other processing techniques.[17,18] In general, the plastic deformation methods used for grain size refinement in Zn alloys may be divided into three groups: hot deformation, cold deformation, and severe plastic deformation (SPD) processes. The mechanical properties of selected high-strength (YS > 200 MPa and UTS > 300 MPa) Zn alloys, together with information about their processing methods and applied strain rates during RT tensile tests, are summarized in Table I where these examples are grouped depending on the final processing temperature. These results lead to three main conclusions: (1) Mg, Li, and Cu are the most effective alloying elements in strengthening Zn alloys via grain refinement and precipitation hardening through the formation of $Zn_{11}Mg_2$, Zn_2Mg, Zn_4Li and Zn_4Cu phases, respectively; (2) the hot processing of Zn alloys

produces materials meeting the strength requirements but often without the required plasticity; (3) cold processing directly after annealing or as a final step of complex processing provides significantly higher ductility in high-strength Zn alloys.

Except for the brittle Zn-1.6Mg alloy attained after ECAP, other Zn alloys processed by SPD were not included in Table I because most studies lead to highly ductile but insufficiently strong ultrafine-grained Zn-based materials.[14,30–32]

The objective of this research was to examine the characteristics and properties of high-strength, ductile Zn-based materials fabricated by processing using hot, cold, and SPD techniques. Accordingly, a newly designed Zn-3Ag-0.5Mg alloy, a potentially biodegradable material for cardiovascular applications, was fabricated and subjected to hot extrusion, hot extrusion followed by cold rolling and high-pressure torsion at RT.

II. EXPERIMENTAL MATERIAL AND PROCEDURES

A. Materials Processing

The Zn-3Ag-0.5Mg alloy (wt pct) was fabricated by melting pure zinc (99.995 wt pct), silver (99.995 wt pct), and magnesium (99.95 wt pct) at 650 °C in a graphite crucible for 30 minutes using an induction furnace, followed by gravity casting into a steel mold. The ϕ 20 mm × 80 mm ingot was annealed at 350 °C for 4 hours to homogenize the microstructure and then water-cooled. The precise chemical composition was measured using Energy Dispersive X-ray Spectrometry (EDS) using an FEI VERSA 3D scanning electron microscope (SEM) equipped with an EDAX microanalysis system. The composition was determined based on spectra collected at 20 keV and analyzed by EDAX Genesis software utilizing ZAF correction and averaging several selected areas. The measured weight contents of Ag and Mg were 2.99 ± 0.03 wt pct and 0.54 ± 0.04 wt pct, respectively, which is close to the nominal chemical composition.

The annealed alloy was subjected to three different deformation processes. First, hot extrusion (HE) was performed at 250 °C with an extrusion speed of 0.1 mm/s and an extrusion ratio of 25:1 to obtain ϕ 4 mm rods. Second, cold rolling (CR) was carried out on the hot-extruded material in a direction parallel to the rod axis to avoid cracking the coarse-grained annealed billet. This process was performed with a thickness reduction up to 75 pct at a constant rolling speed of 0.06 m/s. Third, high-pressure torsion (HPT) was performed at RT under quasi-constrained conditions[33] with a constant rotation speed of 1 rpm. The annealed samples with a diameter of 9.8 mm and a thickness of 0.85 mm were processed under an applied pressure of 6.0 GPa through 5 turns to obtain a reasonably homogenous microstructure.

Table I. Mechanical Properties of Selected High-Strength Zn Alloys

Deformation Process	Composition (Wt Pct)	Strain Rate (s^{-1})	YS (MPa)	UTS (MPa)	Elongation (Pct)	Reference
Hot Deformation Processes						
Hot Rolling	Zn-0.2Li	1×10^{-3}	245 ± 7	369 ± 18	14 ± 2	Zhao et al.[19]
	Zn-0.4Li		430 ± 14	448 ± 2	14 ± 3	
	Zn-0.7Li		476 ± 51	468 ± 4	2.0 ± 0.3	
Hot Rolling	Zn-0.8Li-0.2Mg	no details	254 ± 5	341 ± 5	31 ± 6	Zhang et al.[20]
Hot Extrusion	Zn-3Cu-1Mg	1×10^{-3}	427	441	0.9	Tang et al.[21]
Hot Extrusion	Zn-1.2Mg	1mm/min (~ 3.3×10^{-4}*)	220 ± 15	363 ± 5	21 ± 5	Shen et al.[22]
Equal-Channel Angular Pressing	Zn-1.6Mg	1.1×10^{-3}	361	423	5.2	Liu et al.[23]
Cold Deformation Processes						
Hot Extrusion + Cold Drawing	Zn-0.02Mg	1×10^{-3}	388 ± 2	455 ± 2	5.4 ± 0.3	Wang et al.[24]
Hot Extrusion + Cold Drawing	Zn-0.08Mg after 0 days	3.3×10^{-3}	250	266	30	Jin et al.[25]
	Zn-0.08Mg after 1 year	3.3×10^{-3}	383 ± 6	434 ± 6	3.5 ± 0.5	
	Zn-0.08Mg after 1 year	1×10^{-3}	337	374	34	
Hot Extrusion + Hydrostatic Extrusion	Zn-1Mg	8×10^{-3}	316	435	35	Jarzębska et al.[26]
Cold Rolling	Zn-0.5Cu-0.05Mg	2×10^{-3}	241 ± 5	312 ± 2	44 ± 2	Ardakani et al.[27]
Hot Rolling + Cold Rolling	Zn-4Cu	1 mm/min	327	393	39	Li et al.[28]
Hot-Warm (100 °C) Rolling	Zn-0.8Li	3.3×10^{-4}	261	401	80	Li et al.[29]

*Assuming 5-fold specimens according to preparation mentioned in paper based on ASTM E8/E8M-11 standard method.

B. Microstructural Characterization

Microstructural observations of samples in the as-cast, annealed, HE, CR, and HPT states were performed using an SEM equipped with EDS and EDAX Electron Back-Scattered Diffraction (EBSD) detectors. All samples were prepared by grinding with SiC papers to #2000 grit and polishing using 3 and 1 μm water-free diamond suspensions. To remove the residual scratches and deformed layer, low-angle Ar^+ ion polishing was performed at 2.5 kV for 45 minutes. The observations of the as-cast and annealed samples were performed on the cross-sections and the plastically deformed samples were examined on longitudinal sections. Schematic illustrations of the alloy processing routes and the sample preparation are given in Figure 1.

Lamellae from the extruded Zn-3Ag-0.5Mg alloy were prepared using an FEI Quanta 3D 200i SEM equipped with a focused ion beam (FIB) facility and analyzed using an FEI Tecnai TF 20 X-TWIN transmission electron microscope (TEM). For phase identification, EDS data were combined with selected area electron diffraction (SAED) patterns and then analyzed utilizing JEMS software. The EDAX EBSD system and TSL OIM™ software were used to acquire and analyze the crystallographic orientation maps. In order to obtain an optimal number of grains for further analysis, EBSD maps of either 120×120 μm^2 or 15×15 μm^2 were acquired with step sizes of either 150 nm (HE, CR) or 30 nm (HPT), respectively.

The average grain size, crystallographic orientation maps, texture, and grain boundary misorientation distributions were analyzed using the MTEX toolbox in Matlab™. A single grain was defined as a set of at least 5 points with a misorientation angle between neighboring grains higher than 15 deg. The misorientation angle for subgrains was set within the range of 3 to 15 deg. Only grains of the Zn-based matrix were considered and the precipitates of other phases were excluded from the analysis. Additionally, the phase composition was examined using a Panalytical Empyrean X-ray diffractometer with CuKα radiation ($\lambda = 1.54$ Å). Diffractograms were collected in the 20 to 90 deg range of 2θ angles at 40 kV, 40 mA, with a scanning rate of 0.4 deg/min and a step size of 0.02 deg. The XRD patterns were analyzed using TOPAS[34] software and Rietveld analysis.[35]

C. Mechanical Properties Testing

Tensile tests for materials after HE, CR, or HPT were conducted at RT using an Instron 5966 universal testing machine with initial strain rates of 10^{-4}, 10^{-3}, and 10^{-2} s^{-1}. Tensile specimens were machined from the extruded rods in HE to obtain gauge lengths and diameters equal to 30 and 3 mm, respectively. Wire electro-discharge machining was used to cut dog-bone type flat specimens with gauge sections of about $16 \times 2 \times 1$ mm^3 along the rolling direction after CR and also to cut
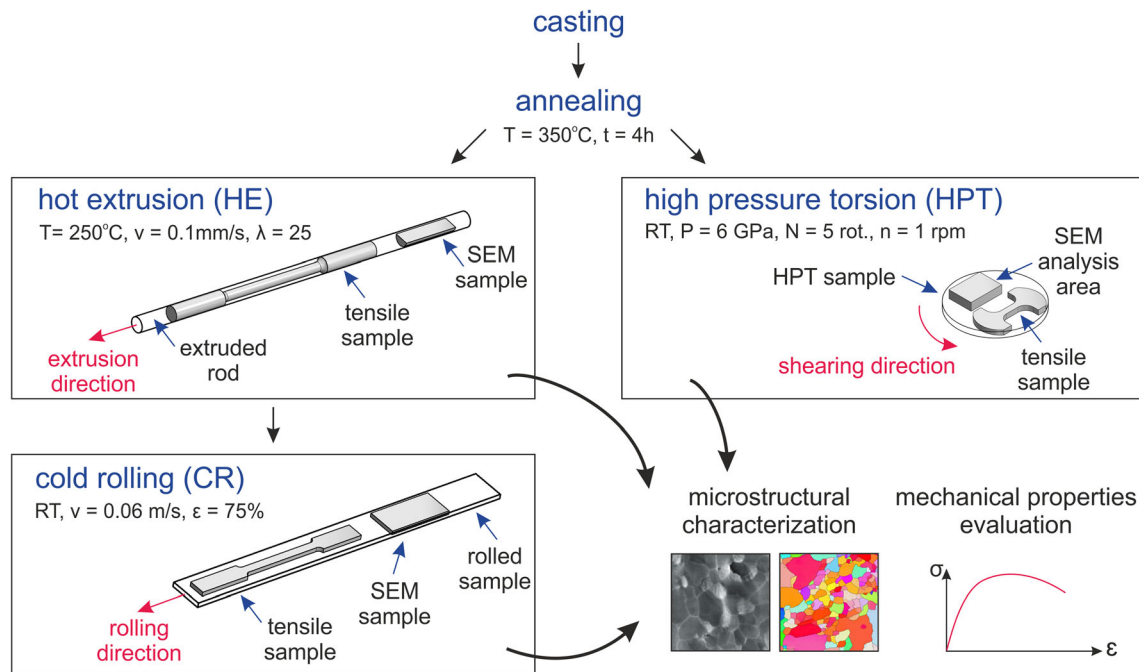
Fig. 1—Schematic of processing routes of the Zn-3Ag-0.5Mg alloy showing sections used for SEM-EBSD analysis and geometry of tensile samples. Note that the scale in the sample drawings was not preserved.

micro-specimens after HPT with 1.5 mm gauge lengths and gauge sections of 0.6×0.7 mm^2. Based on the recorded force-displacement curves and equipment specifications, the measurement uncertainties were calculated for the measured yield stress, ultimate tensile stress, and elongation to failure.[36]

III. EXPERIMENTAL RESULTS

A. Microstructure of the Initial Material

In Figure 2, the microstructures and elemental information for the Zn-3Ag-0.5Mg alloy are shown for (a, c, e) the as-cast and (b, d, f) the annealed states. After casting, the material exhibits a dendritic morphology with a characteristic lamellar eutectic mixture in the interdendritic regions. The SEM-EDS elemental mapping in Figure 2(c) confirms the presence of Ag within the dendrites, probably existing as a dissolved element in Zn, and there is an increased concentration of Mg within the interdendritic regions. The main peaks on the X-ray diffractogram in Figure 2(e) originate from the η-Zn matrix phase. According to binary phase diagrams,[37] the maximum solubility of Ag and Mg in liquid Zn is 3 and 0.1 pct, respectively. It was observed during Rietveld analysis that peaks related to η-Zn exhibit slightly different positions and the c/a ratio of the η-Zn in the alloy is different by comparison with pure Zn.[38] Thus, dissolved Ag atoms decrease the interplanar distance in the Zn crystal cell in the c-axis and generally lead to an increase in the c/a ratio of the η-Zn phase with increasing amounts of Ag.[39] This

suggests the presence of Ag and most likely small amounts of Mg in the η-Zn solid solution. A few peaks of relatively low intensity and the broadening of some peaks belonging to the η-Zn phase suggest the presence of a small fraction of secondary phases in the alloy. During indexing of the diffraction peaks, all possible phases in the Zn-Ag and Zn-Mg systems were considered and it was found that secondary phases in the alloy correspond to Zn_2Mg and probably ε-Zn_3Ag. The Zn_2Mg phase, together with the η-Zn phase, is a constituent of the eutectic mixture observed in the interdendritic regions.

After annealing, the dendritic structure was transformed into large equiaxed grains and it is apparent from the SEM-EDS elemental maps in Figure 2(d) that Ag is more uniformly distributed within the sample. According to the Zn-Ag phase diagram for a concentration of 3 pct Ag,[37] after rapid water cooling from 350 °C Ag forms a supersaturated solid solution with Zn of the η-Zn phase. In place of the lamellar eutectic mixture, coagulated grains of Mg-rich second phase form along the primary dendritic boundaries. In addition, the EDS point analyses marked with yellow crosses in Figure 2(d) indicate that the average atomic concentrations of Mg, Ag, and Zn in these grains are about 15 pct, 3 pct, and 82 pct, respectively. The corresponding X-ray diffractogram in Figure 2(f) supports a phase transformation from a η-Zn $+$ Zn_2Mg eutectic mixture to a $Zn_{11}Mg_2$ phase enriched in Ag. It should be noted that the possibility of a small fraction of ε-Zn_3Ag phase in the microstructure in the annealed state cannot be excluded.
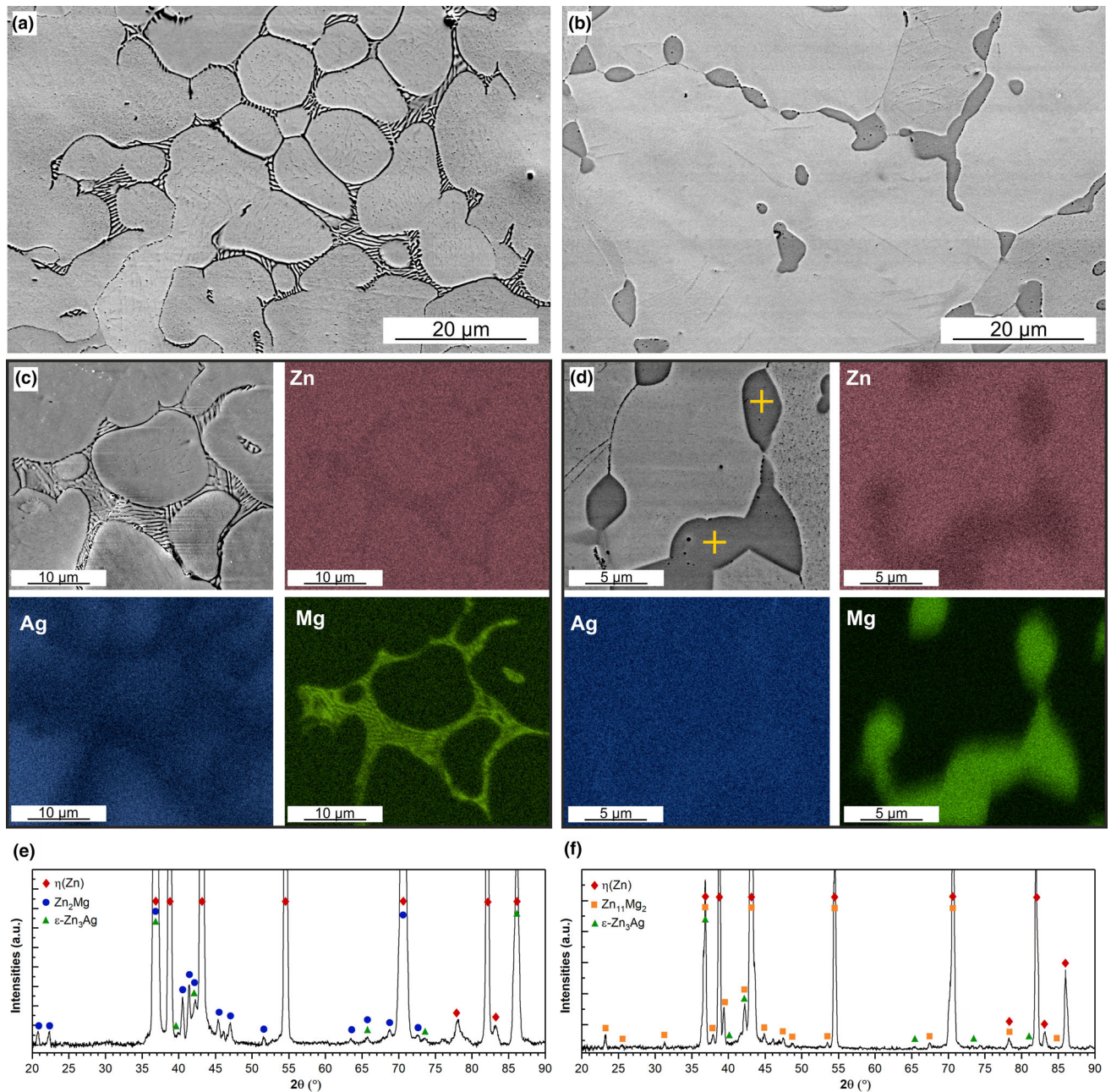
Fig. 2—Microstructures (*a*), (*b*), EDS elemental maps (*c*), (*d*), and X-ray diffractograms (*e*), (*f*) of the as-cast ((a), (c), (e)) and annealed ((b), (d), (f)) Zn-3Ag-0.5Mg alloy.

B. *Microstructures After Plastic Deformation Processes*

The microstructures of the annealed material after processing through the three different deformation processes are shown in Figure 3 where (a, d) is for HE, (b, e) is for CR, and (c, f) is for HPT. It can be seen in Figures 3((d) to (f)) that the grain size is significantly refined for all three processing routes. Similar to the annealed state, the bright grains of the η-Zn matrix phase are located mostly at the grain boundaries, whereas the grains of the Mg-rich phase marked with red arrows remain in the microstructure. Additionally, precipitates of another intermetallic phase marked with yellow arrows are visible in the form of small white

particles. It is reasonable to assume that the presence of precipitates hinders grain growth after dynamic recrystallization, most probably during the processing, together with the breaking of the Mg-rich grains under the applied external stress.

The Mg-rich grains are visible as white grains in Figures 3((a) to (c)) as observed using the secondary electron mode in the SEM and these grains are distributed vertically in the HE and CR samples corresponding to the extrusion (ED) and rolling (RD) directions, respectively. It appears that other small precipitates are more randomly dispersed both at grain boundaries and within the η-Zn grains. For the HPT
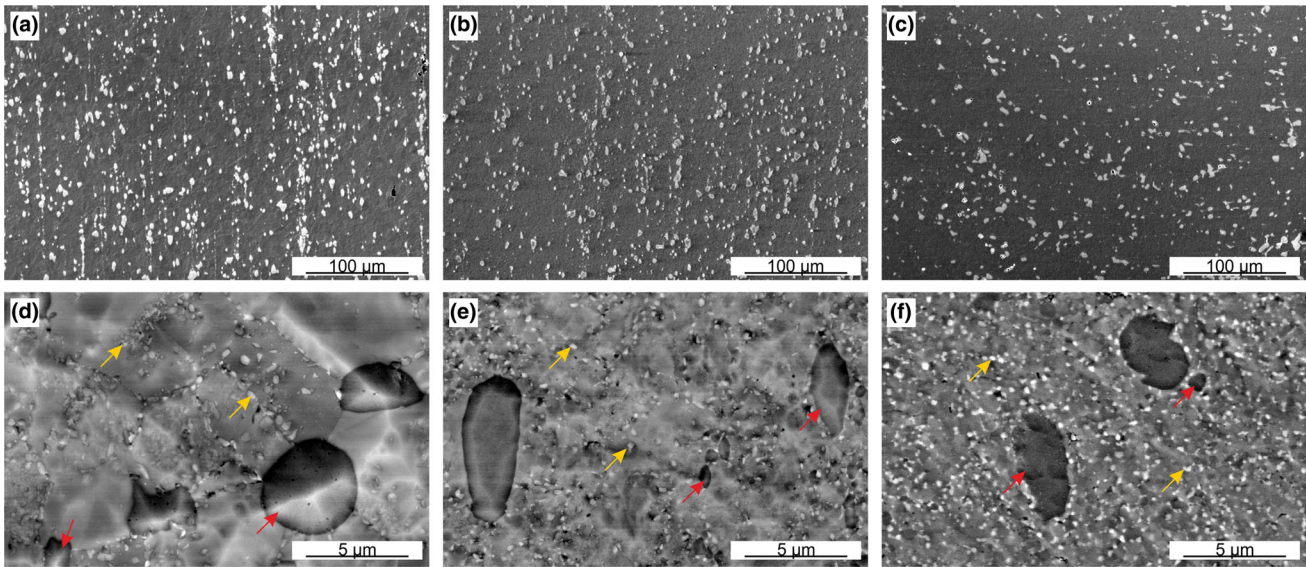
Fig. 3—Microstructures of the hot extruded (*a*), (*d*), cold rolled (*b*), (*e*) and HPT (*c*), (*f*) Zn-3Ag-0.5Mg alloy: SEM-SE (a) to (c), SEM-BSE (d) to (f). Yellow and red arrows indicate the newly precipitated phase and Mg-rich phase, respectively.

sample shown in Figure 3(c), all precipitates are distributed uniformly within the η-Zn matrix. The volume fractions of this Mg-rich phase were estimated as 10.8, 10.4, and 8.8 pct for HE, CR, and HPT, respectively, where this is consistent with the volume fraction determined for the annealed state which was equal to 10.1 pct. The slight differences in the topology of the samples shown in Figures 3((d) to (f)) are due to variations arising from the metallographic preparation process.

Based on the Zn-Ag and Zn-Mg phase diagrams,[37] no phase transformations are expected below the highest temperature of 250 °C applied during processing. Therefore, an XRD analysis was performed to identify the phases present in the HE sample. The XRD diffractogram of the HE sample in Figure 4 confirms the presence of η-Zn, $Zn_{11}Mg_2$, and ε-Zn_3Ag phases in the microstructure but additional peaks of other intermetallic phases were not detected probably due to texturing after extrusion and their small volume fractions. Therefore, SEM-EDS and TEM analyses were performed and Figure 5(a) shows the SEM-SE image of the extruded sample with the corresponding SEM-EDS elemental distribution maps. As in the annealed state, Mg occurs mainly in the larger grains composed of the $Zn_{11}Mg_2$ phase and the small precipitates are enriched in Ag.

Phase identification of these small precipitates was performed based on TEM observations and SAED patterns shown in Figure 5((b) and (c)). It can be seen in Figure 5(b) that the micrometric Mg-rich grains are composed of nanosized particles which are much smaller than 100 nm. The SAED pattern indicates a mixture of the $Zn_{11}Mg_2$ phase and fine precipitates of the Zn_2Mg phase where these phases are identified based on spot and ring diffraction patterns, respectively. Using STEM-EDS analysis performed on a few points marked with red crosses in Figure 5(b), the average chemical composition (at. pct) was close to 87 pct Zn, 3 pct Ag,
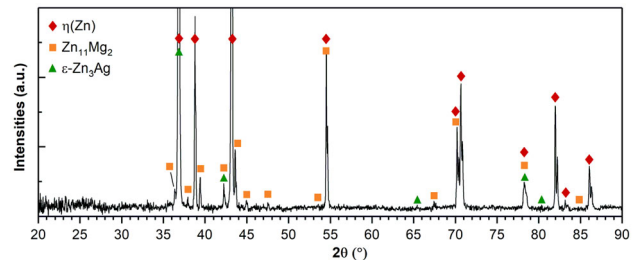

Fig. 4—X-ray diffractogram of the hot extruded Zn-3Ag-0.5Mg alloy.

and 10 pct Mg, thereby suggesting that Ag occurs in the Mg-rich regions so that these phases are more complex with partial substitution of Ag. In addition, it was confirmed that the small precipitates observed within the η-Zn grains and at grain boundaries do not contain Mg and belong instead to the ε-Zn_3Ag phase. The average atomic concentrations of the points marked with yellow crosses in Figure 5(c) were approximately 82 pct Zn and 18 pct Ag and the average size of the ε-Zn_3Ag precipitates was measured within the range of a few dozen to a few hundred nm.

C. SEM-EBSD Analysis

Measurements by EBSD were used to examine the grain size and grain orientations after processing. Figure 6 shows EBSD-IPF orientation maps and misorientation angle distributions of samples after (a,d) HE, (b,e) CR and (c,f) HPT. All three conditions show grain refinement compared with the annealed state and Table II summarizes the average grain sizes and the densities of high-angle (HAGB) and low-angle (LAGB) grain boundaries. The largest grain size was 6.0 ± 2.5 μm after HE but this was reduced to 1.8 ± 1.4 μm by CR and then to 1.2 ± 1.1 μm after HPT. Subgrains visible in
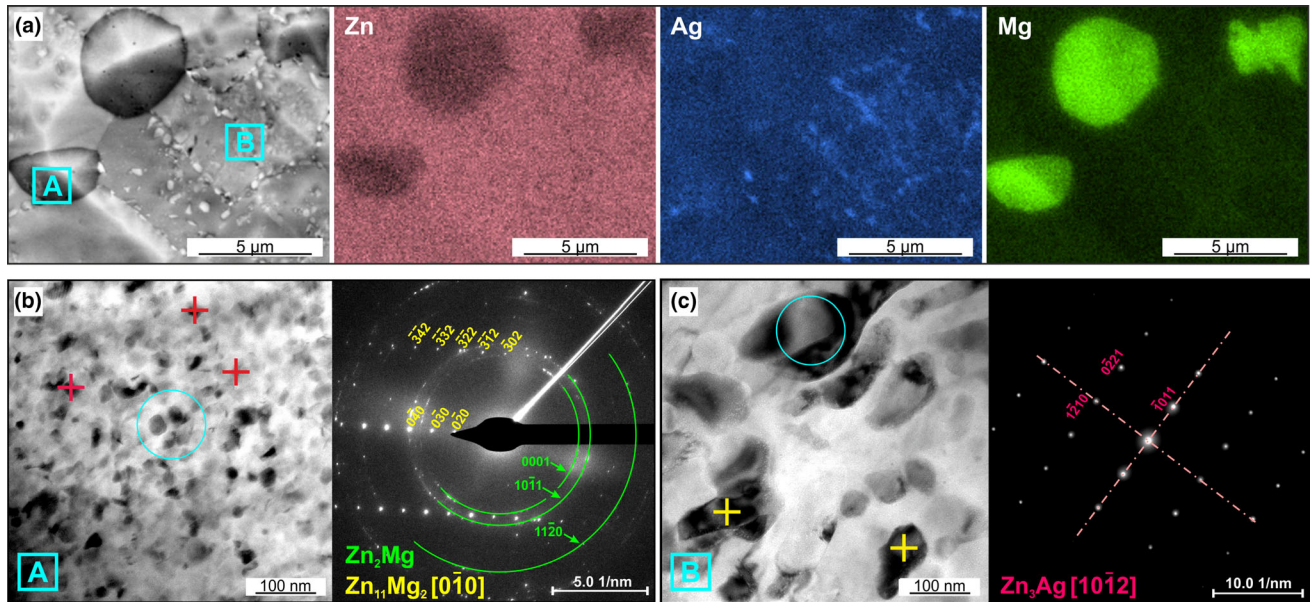
Fig. 5—SEM-BSE image and SEM-EDS elemental maps for element distributions in the investigated areas of extruded Zn-3Ag-0.5Mg alloy (*a*), SEM. TEM bright-field images and SAED patterns corresponding to Mg-rich grains similar to the area [A] (*b*) and Ag-rich precipitates similar to the area [B] (*c*) marked in (*a*).
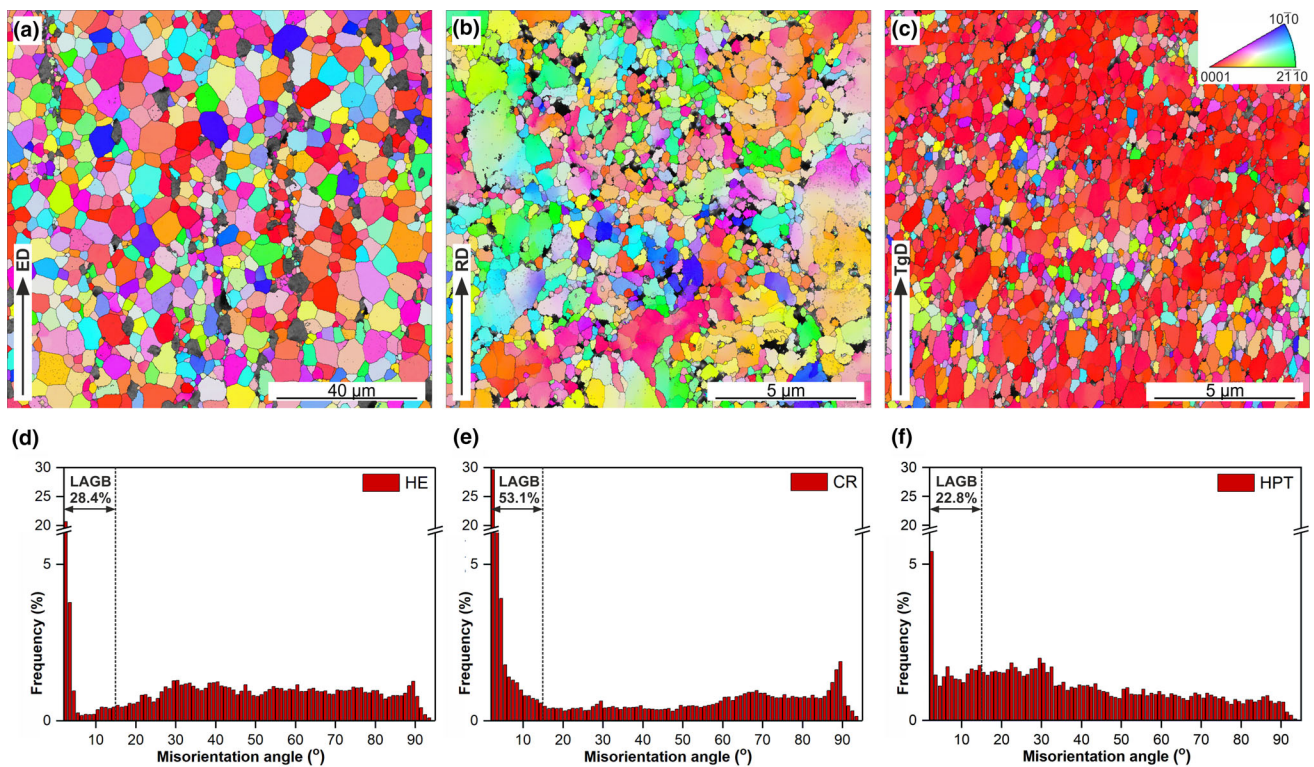

Fig. 6—EBSD-IPF orientation maps (*a*) to (*c*) and distribution of grain boundary misorientation angles (*d*) to (*f*) for Zn-3Ag-0.5Mg alloy after HE ((a), (d)), CR ((b), (e)) and HPT ((c), (f)). Please pay attention to different scale bars in maps (a) to (c). *ED*, extrusion direction; *RD*, rolling direction; *TgD* tangential direction.

the CR and HPT samples were about one-half of the grain size. Most grains were oriented in [0001] directions after HPT but they were more randomly oriented after HE and CR.

The grain boundary misorientation angle distributions are plotted in Figure 6((d) to (f)) and in the CR sample a peak is visible at ~ 87 ± 3 deg related to the presence of twin boundaries. These distributions are

consistent with the calculated densities of HAGBs and LAGBs in Table II. The density of LAGBs relates to the subgrain structure and increases significantly after CR. By contrast, the highest density of HAGBs occurs in the HPT sample, which is typical for SPD processing.[40]

D. Texture Analysis

Crystallographic texture analysis was performed based on (0002), $(10\bar{1}0)$ and $(11\bar{2}0)$ pole figures recalculated from the EBSD data. These data were measured on sample planes parallel to ED, RD and the shearing plane in the HE, CR, and HPT samples, respectively, as presented in Figure 1. Figure 7 shows the characteristic textures typical for anisotropic hexagonal close-packed (HCP) metals after (a) HE, (b) CR, and (c) HPT.

The HE sample exhibits a $(10\bar{1}0)$ fiber texture with the (0002) and $(11\bar{2}0)$ poles more randomly distributed and with a texture that is axially symmetric. The lowest maximum intensities were recorded in this case. This texture is usually a result of the activation of basal slip systems during extrusion as is typical for HCP metals while the prismatic planes are perpendicular to the ED.[41,42]

In the texture for the CR sample, the maximum intensity of the (0002) pole figure is split into two maxima and tilted towards the RD. Typically, for rolled pure Zn, the $(11\bar{2}0)$ pole aligns with the RD and the $(10\bar{1}0)$ pole is parallel to the transverse direction (TD). For the Zn-3Ag-0.5Mg alloy, the maxima are slightly shifted which is probably related to the presence of deformed grains. Such texturing originates from a combination of basal slip and large-scale twinning[43] and this is consistent with the peak observed in Figure 6(e) corresponding to the existence of twin boundaries.

By contrast, the high shear stress in HPT leads to a strong basal texture with the highest maximum intensity of 24 and with many grains with a parallel c-axis. The six maxima visible in the prismatic pole figures with a maximum intensity of 6 relates to the 6-fold symmetry of HCP crystals and the preferred orientations achieved by the crystals during torsional straining in terms of the tangential monotonic shearing direction (TgD). Similar results were reported for Zn-Mg hybrids after 5 turns during HPT where there was no prismatic texture and the alignment of $(10\bar{1}0)$ and $(11\bar{2}0)$ with the radial direction (RdD) was in agreement with the development of a basal texture.[44] Generally, the observed textures of HPT samples are composed of two constituents corresponding to basal and $(0001)[11\bar{2}0]$ textures.[45]

E. Mechanical Properties

Uniaxial tensile tests were conducted to examine the effect of each processing technique on the mechanical properties. Tensile tests were performed at three different strain rates and the results are depicted in Figures 8((a) to (c)) as engineering stress vs engineering strain for the HE, CR, and HPT samples, respectively. To highlight the differences in mechanical properties

after the various processing routes, all results are summarized in Table III.

For the HE samples, the YS and UTS values increase consistently with increasing strain rate but there is no systematic change in the elongations to failure. At the microscopic level, a brittle mode was confirmed during fractographic analysis as shown in Figure 8(d) where the fracture surface has small cleavage facets (marked with white arrows) indicating transgranular fracture through the Zn-based grains.

The application of CR after hot extrusion leads to higher values of the UTS but the values of the YS are lower than in the HE condition. This is caused by the grain size refinement and by the texture present after extrusion, which is more susceptible to tensile deformation. A transformation from brittle to ductile fracture mode was recorded after CR as shown in Figure 8(e) where the fracture surface has numerous spherical dimples and some tearing edges that are consistent with the observed necking and total elongations to failure above 30 pct.

The ultrafine-grained sample after HPT gave the highest UTS of ~516 MPa when straining at 10^{-2} s^{-1} but the values for the UTS at the two lower strain rates were lower than for the CR condition. The most significant differences were recorded for the total elongations in the HPT samples which were much higher than for the CR samples at all three strain rates. Necking was observed at all strain rates and Figure 8(f) shows an example of small spherical and slit-like dimples on the fracture surface. These dimples are significantly deeper than in the rolled state and the elongation to failure was double the value for the CR state. In ductile fracture modes, the ε-Zn$_3$Ag phase precipitates and Mg-rich grains are not responsible for initiating cracks and it appears that other deformation mechanisms, such as grain boundary sliding (GBS),[14] may be responsible for the high ductility in the fine-grained samples.

IV. DISCUSSION

A. Effect of Simultaneous Additions of Silver and Magnesium on the Initial Microstructure

Microstructural investigations reveal that the simultaneous addition of Ag and Mg to pure Zn leads to a multi-phase microstructure in the Zn-3Ag-0.5Mg alloy. According to the Zn-Mg and Zn-Ag phase diagrams,[37] the phases that may appear in equilibrium conditions at RT are the η-Zn solid solution enriched with Ag, ε-Zn$_3$Ag, and Zn$_{11}$Mg$_2$. Nevertheless, it is noted that in the ternary Zn-Mg-Ag system a substitution of Zn and/or Ag sites in the ε-Zn$_3$Ag phase with Mg atoms and Zn and/or Mg sites in the Zn$_{11}$Mg$_2$ phase with Ag atoms may be a possibility. During crystallization, the alloy undergoes a peritectic reaction (L + ε-Zn$_3$Ag → η-Zn) in which the primary ε-Zn$_3$Ag phase is formed. As a result of this reaction together with liquid, there is a partial formation of a η-Zn solid solution.

Table II. Average Grain and Subgrain Size, and Density of HAGB and LAGB After HE, CR, and HPT

Material	Grain Size (μm)	Subgrain Size (μm)	Density of HAGB (μm/μm^2)	Density of LAGB (μm/μm^2)
HE	6.0 ± 2.5	5.5 ± 2.1	0.57	0.21
CR	1.8 ± 1.4	1.0 ± 0.9	3.81	5.75
HPT	1.2 ± 1.1	0.6 ± 0.3	5.46	1.61
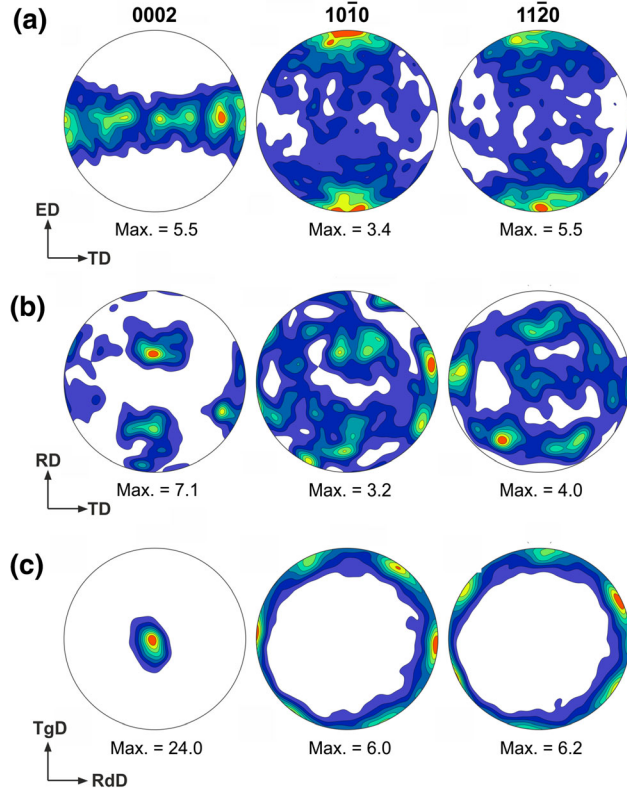
Fig. 7—Basal (0002), and prismatic ($10\bar{1}0$), ($11\bar{2}0$) pole figures of HE (*a*), CR (*b*), and HPT (*c*) samples.

Some local heterogeneities and non-uniform distributions within the η-Zn phase may appear at 3 pct Ag leading to further precipitation of the ε-Zn$_3$Ag phase with decreasing temperature and, as the temperature drops below 364 °C, the remaining Mg-rich liquid undergoes a eutectic reaction. As documented for Zn-0.5Mg alloy,[46] two kinds of competitive eutectic mixtures, of the form Zn + Zn$_{11}$Mg$_2$ and Zn + Zn$_2$Mg, can appear. It was also shown that, due to non-equilibrium solidification, the MgZn$_2$ phase appears in the Zn-1.8 pct Mg alloy.[47] Based on the XRD diffractogram in Figure 2(e), the η-Zn + Zn$_2$Mg eutectic mixture formed in the as-cast state and, as a result of annealing and subsequent water cooling, the eutectic regions transformed to grains of the Zn$_{11}$Mg$_2$ phase enriched in Ag with a morphology similar to the grains reported earlier for the Zn-0.5Mg alloy.[10] Interestingly, a large number of nanometric particles of the Zn$_2$Mg phase precipitated after plastic deformation. This is consistent with the results for a Zn-1.6Mg alloy where

precipitates of the Zn$_2$Mg phase also formed in the larger Zn$_{11}$Mg$_2$ grains after a hot ECAP process.[23]

Precipitation of the ε-Zn$_3$Ag phase occurred either during HE or in the cooling after processing due to the limited solubility of Ag in Zn at 250 °C. It appears that in the sample after CR the phase composition remains the same. The precipitation of the Zn$_2$Mg and ε-Zn$_3$Ag phases may occur as larger plastic strains are applied during HPT processing. According to the STEM-EDS analysis, the Mg-rich phases are enriched in Ag and the similar atomic radii of Ag (144 pm) and Mg (145 pm) suggests that Ag can substitute Mg in these phases.

B. *Effect of Microstructure and Grain Size on Mechanical Behavior*

In polycrystalline HCP materials, deformation begins by slip and, due to insufficient strain accommodation, the slip is accompanied by twinning. The grain size plays a vital role in the activation of twinning. Thus, it was shown that the critical stress for twinning in Zn alloys increases with a decrease in grain size, and the contribution of twinning to the total deformation increases with increasing grain size.[48] As documented for pure Mg,[49] a decrease in grain size below a critical value of ~2.7 μm inhibits twinning and promotes dislocation slip and other deformation mechanisms. The twinning occurring in coarse-grained HCP metals contributes to higher strengthening and lower plasticity than in fine-grained metals and this is consistent with the present results for the HE alloy where this sample exhibits the highest YS for all strain rates. The decrease in YS caused by microstructure refinement in the CR and HPT samples suggests the advent of other mechanisms such as grain boundary sliding (GBS).

It is well known that the size, morphology, and distribution of microstructural features play a significant role in determining the strength and ductility. Typically, hard precipitates located at grain boundaries do not produce reasonable plasticity.[50] However, despite the apparent brittleness of the HE samples, in the CR and HPT states the Mg- and Ag-rich precipitates have similar sizes and morphology but exhibit increased ductility which is probably due to the occurrence of GBS. This flow mechanism will affect the accommodation of external stresses and thereby produce additional deformation instead of brittle fracture.[14] As a result, high-stress zones are formed around the intermetallic precipitates and these will hinder grain movement and act as nucleation sites for new dynamically recrystallized grains, as was observed in a Zn-3Cu-xFe alloy.[51]
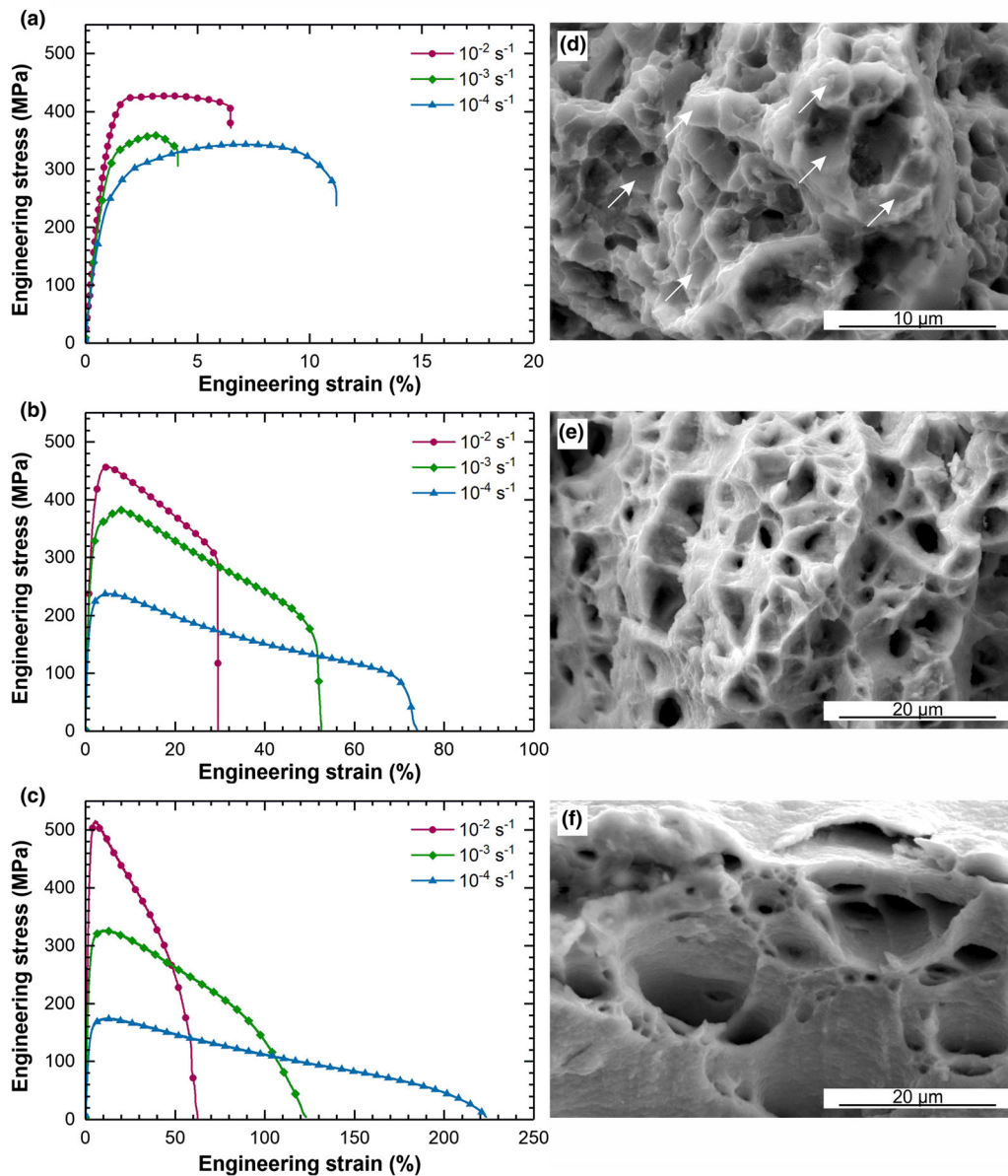
Fig. 8—Engineering strain–stress curves of Zn-3Ag-0.5Mg alloy and fracture morphologies investigated after tensile test conducted at 10^{-3} s^{-1} for HE ((a), (d)), CR ((b), (e)), and HPT ((c), (f)) samples. Please pay attention to different scale bars in figures (d) to (f) and different elongation ranges on the x-axis.

C. Effect of Strain Rate on Mechanical Properties

Zinc is characterized by a low melting temperature and therefore deformation of samples processed at RT may be analyzed using mechanisms associated with elevated temperature tensile testing. Thus, the steady-state strain rate, $\dot{\varepsilon}$, may be expressed by the relationship:

$$\dot{\varepsilon} = \frac{ADGb}{kT} \left(\frac{b}{d}\right)^p \left(\frac{\sigma}{G}\right)^{n'},$$

where A is a dimensionless constant, D is the appropriate diffusion coefficient, G is the shear modulus, b is the Burgers vector, k is Boltzmann's constant, T is the absolute temperature, d is the grain size, σ is the applied stress, p is the inverse grain size exponent, and n' is the stress exponent which is equal to the inverse of the strain rate sensitivity, m.

Based on the UTS in Table III, the values of m were calculated for the strain rate ranges of $10^{-2} - 10^{-3}$ s^{-1} and $10^{-3} - 10^{-4}$ s^{-1} and the results are presented in Figure 9(a). Similarly, the variation of the elongation to failure with strain rate is shown in Figure 9(b). The elongations recorded in this investigation reached a maximum of 220 pct in the HPT sample at a strain rate of 10^{-4} s^{-1} and the associated strain rate sensitivity was $m \approx 0.27$. Thus, these results fail to fulfill the requirements for superplasticity where, by definition, the elongations must be at least as high as 400 pct with a

Table III. Mechanical Properties of Zn-3Ag-0.5Mg Alloy After HE, CR, and HPT with the Measurement Uncertainty Values

	YS (MPa)			UTS (MPa)			Elongation (Pct)		
Strain rate (s^{-1})	10^{-2}	10^{-3}	10^{-4}	10^{-2}	10^{-3}	10^{-4}	10^{-2}	10^{-3}	10^{-4}
HE	362 ± 3	283 ± 3	229 ± 2	427 ± 4	359 ± 4	343 ± 3	6.5 ± 0.8	4.1 ± 0.7	11.2 ± 0.8
CR	321 ± 4	254 ± 4	168 ± 2	456 ± 6	382 ± 5	238 ± 3	30 ± 1	53 ± 1	73 ± 1
HPT	359 ± 12	214 ± 7	113 ± 4	516 ± 13	327 ± 8	175 ± 5	62 ± 2	122 ± 2	224 ± 6
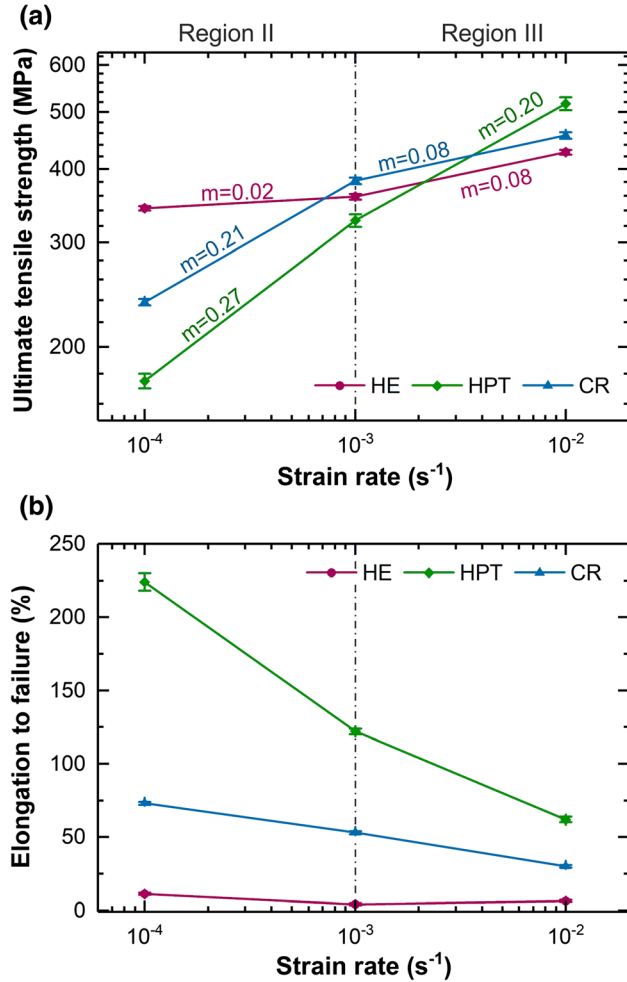
Fig. 9—Variation of the ultimate tensile strength (*a*) and elongation (*b*) vs strain rate.

value of $m \approx 0.5$.[52] The limited elongation and the value of m close to ~ 0.3 obtained for the HPT sample are consistent instead with dislocation glide as the rate-controlling flow process.[53] By contrast, there are some earlier reports documenting true superplastic flow in tensile testing at RT in some ultrafine-grained Zn alloys obtained by SPD processing: for example, elongations of 510 pct in a Zn-0.5Cu alloy,[54] 520 pct in a Zn-5Al alloy, [55] and up to 1000 pct in a Zn-0.3Al alloy.[56]

D. *Implications of These Results for the Production of Cardiovascular Stents*

High flow stress, low yield stress, and therefore high strain hardening ability are desirable when considering materials for stent production. Together with the appropriate ductility, it provides an adequate plastic deformation range within which the stent can be radially expanded inside the vessel, thereby avoiding localized strain concentrations or premature fractures. This is mainly associated with developing resistance to dislocation slip by twin boundaries, high-angle grain boundaries and second-phase particles.[57] The strain hardening exponent, *n*, was estimated from double logarithmic true stress–true strain curves (not presented here) within the uniform plastic deformation ranges for the HE, CR, and HPT samples.

The general observation made for samples after the three deformation methods was that the strain hardening exponent was high at the low strains and then decreased at higher strains. This behavior was observed for all tested strain rates and the changes of *n* between low strain ranges and high strain ranges were most significant, while differences between different strain rates and different materials were much less pronounced. The changes of *n* with strain variation were previously observed in various metals and alloys and the character of these changes was described as being dependent on phase composition and the presence of structural or phase transformations during the deformation.[58] The increased strain hardening exponent in the low strain range was observed in martensitic steels due to Ni_3Al precipitation, followed by decreased *n* at high strains.[59] Similarly, in the currently investigated Zn-3Ag-0.5Mg the initial high *n* value can be explained by dislocation interactions with dispersed Zn_3Ag and $Zn_{11}Mg_2$/Zn_2Mg precipitates (Figure 5). After the initial hardening, the generation rate of new dislocations and the dislocation–precipitate interaction number reaches equilibrium, resulting in a decreased strain hardening exponent. At higher strains in zinc alloys, the dislocation density can be controlled by a relatively high rate of dynamic recovery due to the high homologous temperature of deformation. In addition, as the material is hardened, at higher strains different deformation mechanisms such as GBS become more important resulting in decreased hardening ability and increased plasticity.

For the HE samples, the initial strain hardening exponent *n* was similar at all strain rates and equaled about 0.3. Further straining led to a change of *n* to lower

values, below 0.16, but within a narrow deformation range before the brittle fracture. For comparison, the Zn-0.5Mg extruded alloy with a grain size of 4.1 μm tested at 10^{-3} s^{-1} exhibits a strain hardening exponent equal to 0.22 within the whole uniform plastic deformation range.[10] The higher n value obtained in the same conditions for the Zn-3Ag-0.5Mg alloy can result from the presence of dispersed precipitates, whereas in the microstructure of the Zn-0.5Mg alloy there are $Zn_{11}Mg_2$ particles which are located mostly at grain boundaries. The additional strain hardening effect in the Zn-3Ag-0.5Mg alloy can result from Ag solid solubility in the Zn matrix. On the other hand, the analyzed strain hardening behavior stands in contrast to the results shown for quasi-single-phase extruded Zn-0.8Ag alloy with a grain size of 50.3 μm, where increasing strain caused the increase in the strain hardening exponent from 0.07 to 0.22.[14] That observation was explained by the twinning deformation in the first stage resulting in decreased initial strain hardening, followed by an increase of n due to strong dislocation–twin interactions in the second stage. In the current study, twinning is still possible in coarse grains; however, the much lower average grain size (6.0 $\pm$ 2.5 μm) decreases the ability of twinning to act as a primary strain accommodation mechanism and removes the possibility of decreased n at the onset of deformation. By contrast, the presence of second-phase precipitates and solid solution strengthening due to higher Ag content in the Zn-3Ag-0.5Mg alloy leads to a stronger strain hardening in the first stage of deformation.

In the CR samples, at the first stage, strain hardening occurred with n having values from 0.29 to 0.39 at 10^{-4} s^{-1} and 10^{-2} s^{-1}, respectively. Similarly to HE, this is generally associated with an increase in the dislocation density during deformation and dislocation–precipitate interactions. At higher strains, n decreases to values between 0.15 and 0.09 with decreasing strain rate. As presented in Figure 6(b), the microstructure of the Zn-3Ag-0.5Mg alloy after CR consists of grains with a wider size distribution, and the overall distribution is shifted towards a more refined microstructure. A smaller grain size and higher grain boundary density allow the GBS to contribute much more to the overall deformation behavior, resulting in increased plasticity and a decreased hardening exponent especially at lower strain rates.

The samples after HPT processing exhibit the largest strain hardening exponent in the low strain range in comparison to the HE and CR samples. Initially, the n exponent reaches 0.50 at 10^{-2} s^{-1} and about 0.46 at lower strain rates and then decreases to about 0.11 in the high strain region. High n values are associated with a strong basal texture (Figure 7(c)) and the large fraction of HAGB with misorientation angles below 30 deg (Figure 7(f)). In this case, a relatively sharp basal texture results in a quicker dislocation pile-up and thus a higher strain hardening exponent in the initial deformation stage. Further straining leads to an increase in dislocation density, possibly followed by dynamic recrystallization which can introduce changes in grain boundary structures and increase of the average boundary

misorientation angle. Consequently, the ultra-fine-grained HPT specimens at higher strains became more prone to GBS because of the higher fraction of high-energy grain boundaries providing very high plasticity.[60] Similar results were also reported for ultra-fine-grained pure Zn,[61] Zn-0.5Cu,[62] and the Zn-22Al eutectoid alloy[63] after processing by HPT.

As mentioned earlier, it is crucial for a material under consideration for stent production to exhibit a strain hardening ability within the required range of deformation. In the CR and HPT samples, the hardenability was recorded in a significantly wider strain range than in the HE samples where this is mostly related to the smaller grain sizes and higher densities of grain boundaries. Ideally, the transition from strain hardening to strain softening should be avoided, and based on results presented for the Zn-1Cu[64] and Zn-4Ag-0.6Mn[65] alloys this may be addressed by additional heat treatment after cold deformation processes. In fact, the observed differences in strain hardening exponent n between the tested specimens may be affected by several factors such as grain size, strain level (as discussed above), strain rate, texture, and grain boundary character distribution.

An appraisal of all data obtained from this investigation shows that processing by HE, CR, and HPT provide materials that have reasonable properties for the production of biomedical stents. Nevertheless, it appears that the ductile CR samples are especially attractive for meeting the requirements for use in cardiovascular applications. Thus, the average grain size is ~ 2 μm, and there is a favorable rolling texture, a YS of ~ 254 MPa at a strain rate of 10^{-3} s^{-1}, a corresponding UTS close to ~ 400 MPa, and reasonable values for the strain rate sensitivity and strain hardening exponent.

V. SUMMARY AND CONCLUSIONS

1. This work focused on processing a high-strength ductile Zn-3Ag-0.5Mg alloy via hot, cold, and severe plastic deformation techniques and identifying the factors influencing the flow properties.
2. A high strength but relatively brittle Zn alloy was obtained by hot extrusion. The additional application of cold rolling after HE gave a significantly enhanced ductility and a negligible decrease in the yield and flow stress. Processing by HPT gave a very high strength and excellent elongations to failure but with a relatively high strain rate sensitivity.
3. The optimum processing condition for the production of cardiovascular stents appears to be cold rolling after HE where there is a reasonable yield stress and ultimate tensile stress, and good values for the strain rate sensitivity and strain hardening exponent. The results appear to satisfy the listed requirements for short-term biomedical implants but further research will be needed to evaluate the biodegradation behavior and relevant biological aspects.

REFERENCES

1. G. Li, H. Yang, Y. Zheng, X.-H. Chen, J.-A. Yang, D. Zhu, L. Ruan, and K. Takashima: *Acta Biomater.*, 2019, vol. 97, pp. 23–45.
2. P.K. Bowen, J. Drelich, and J. Goldman: *Adv. Mater.*, 2013, vol. 25, pp. 2577–82.
3. J.C.T. Farge: McGill University Montreal, Canada, 1999.
4. J. Li, W. Xu, X. Wu, H. Ding, and K. Xia: *Mater. Sci. Eng. A*, 2011, vol. 528, pp. 5993–8.
5. E.O. Hall: *Proc. Phys. Soc. Sect. B*, 1951, vol. 64, pp. 747–53.
6. N. Balasubramanian and T.G. Langdon: *Metall. Mater. Trans. A*, 2016, vol. 47A, pp. 5827–38.
7. M. Wątroba, W. Bednarczyk, J. Kawałko, and P. Bała: *Mater. Charact.*, 2018, vol. 142, pp. 187–94.
8. M. Sikora-Jasinska, E. Mostaed, A. Mostaed, R. Beanland, D. Mantovani, and M. Vedani: *Mater. Sci. Eng. C*, 2017, vol. 77, pp. 1170–81.
9. Z. Tang, J. Niu, H. Huang, H. Zhang, J. Pei, J. Ou, and G. Yuan: *J. Mech. Behav. Biomed. Mater.*, 2017, vol. 72, pp. 182–91.
10. E. Mostaed, M. Sikora-Jasinska, A. Mostaed, S. Loffredo, A.G. Demir, B. Previtali, D. Mantovani, R. Beanland, and M. Vedani: *J. Mech. Behav. Biomed. Mater.*, 2016, vol. 60, pp. 581–602.
11. N. Hansen: *Scr. Mater.*, 2004, vol. 51, pp. 801–06.
12. S. Thangaraju, M. Heilmaier, B.S. Murty, and S.S. Vadlamani: *Adv. Eng. Mater.*, 2012, vol. 14, pp. 892–97.
13. Z. Liu, F. Wang, D. Qiu, J.A. Taylor, and M. Zhang: *Metall. Mater. Trans. A*, 2013, vol. 44A, pp. 4025–30.
14. W. Bednarczyk, M. Wątroba, J. Kawałko, and P. Bała: *Mater. Sci. Eng. A*, 2019, vol. 748, pp. 357–66.
15. L. Sun, J. Bai, F. Xue, L. Tao, C. Chu, and J. Meng: *Mater. Des.*, 2017, vol. 135, pp. 267–74.
16. M. Wątroba, W. Bednarczyk, J. Kawałko, K. Mech, M. Marciszko, G. Boelter, M. Banzhaf, and P. Bała: *Mater. Des.*, 2019, vol. 183, p. 108154.
17. J. Venezuela and M.S. Dargusch: *Acta Biomater.*, 2019, vol. 87, pp. 1–40.
18. Y. Qin, P. Wen, H. Guo, D. Xia, Y. Zheng, L. Jauer, R. Poprawe, M. Voshage, and J.H. Schleifenbaum: *Acta Biomater.*, 2019, vol. 98, pp. 3–22.
19. S. Zhao, C.T. McNamara, P.K. Bowen, N. Verhun, J.P. Braykovich, J. Goldman, and J.W. Drelich: *Metall. Mater. Trans. A*, 2017, vol. 48A, pp. 1204–15.
20. Y. Zhang, Y. Yan, X. Xu, Y. Lu, L. Chen, D. Li, Y. Dai, Y. Kang, and K. Yu: *Mater. Sci. Eng. C*, 2019, vol. 99, pp. 1021–34.
21. Z. Tang, H. Huang, J. Niu, L. Zhang, H. Zhang, J. Pei, J. Tan, and G. Yuan: *Mater. Des.*, 2017, vol. 117, pp. 84–94.
22. C. Shen, X. Liu, B. Fan, P. Lan, F. Zhou, X. Li, H. Wang, X. Xiao, L. Li, S. Zhao, Z. Guo, Z. Pu, and Y. Zheng: *RSC Adv.*, 2016, vol. 6, pp. 86410–19.
23. H. Liu, H. Huang, Y. Zhang, Y. Xu, C. Wang, J. Sun, J. Jiang, A. Ma, F. Xue, and J. Bai: *J. Alloys Compd.*, 2019, vol. 811, p. 151987.
24. L. Wang, Y. He, H. Zhao, H. Xie, S. Li, Y. Ren, and G. Qin: *J. Alloys Compd.*, 2018, vol. 740, pp. 949–57.
25. H. Jin, S. Zhao, R. Guillory, P.K. Bowen, Z. Yin, A. Griebel, J. Scha, E.J. Earley, J. Goldman, and J.W. Drelich: *Mater. Sci. Eng. C*, 2018, vol. 84, pp. 67–79.
26. A. Jarzębska, M. Bieda, J. Kawałko, Ł. Rogal, P. Koprowski, K. Sztwiertnia, W. Pachla, and M. Kulczyk: *Mater. Lett.*, 2018, vol. 211, pp. 58–61.
27. M.S. Ardakani, E. Mostaed, M. Sikora-Jasinska, S.L. Kampe, and J.W. Drelich: *Mater. Sci. Eng. A*, 2020, vol. 770, p. 138529.
28. P. Li, W. Zhang, J. Dai, A.B. Xepapadeas, E. Schweizer, D. Alexander, L. Scheideler, C. Zhou, H. Zhang, G. Wan, and J. Geis-Gerstorfer: *Mater. Sci. Eng. C*, 2019, vol. 103, p. 109826.
29. Z. Li, Z.-Z. Shi, Y. Hao, H.-F. Li, X.-F. Liu, A.A. Volinsky, H.-J. Zhang, and L.-N. Wang: *J. Mater. Sci. Technol.*, 2019, vol. 35, pp. 2618–24.
30. W. Bednarczyk, M. Wątroba, J. Kawałko, and P. Bała: *Mater. Sci. Eng. A*, 2019, vol. 759, pp. 55–58.
31. P. Kumar, C. Xu, and T.G. Langdon: *Mater. Sci. Eng. A*, 2006, vol. 429, pp. 324–28.
32. B. Srinivasarao, A.P. Zhilyaev, T.G. Langdon, and M.T. Pérez-Prado: *Mater. Sci. Eng. A*, 2013, vol. 562, pp. 196–202.
33. R.B. Figueiredo, P.R. Cetlin, and T.G. Langdon: *Mater. Sci. Eng. A*, 2011, vol. 528, pp. 8198–204.
34. A.A. Coelho: *Bruker AXS GmbH, Karlsruhe, Germany.*.
35. H.M. Rietveld: *J. Appl. Crystallogr.*, 1969, vol. 2, pp. 65–71.
36. W. Gabauer: *The Determination of Uncertainties in Tensile Testing. Manual of Codes of Practice for the Determination of Uncertainties in Mechanical Tests on Metallic Materials*, 2000.
37. H. Baker, ed.: *ASM Handbook: Alloy Phase Diagrams. Volume 3*, ASM International, New York, 1998.
38. M.H. Yoo: *Metall. Trans. A*, 1981, vol. 12, pp. 409–18.
39. T. Gómez-Acebo: *CALPHAD*, 1998, vol. 22, pp. 203–20.
40. R.Z. Valiev, Y. Estrin, Z. Horita, T.G. Langdon, M.J. Zehetbauer, and Y. Zhu: *JOM*, 2016, vol. 68, pp. 1216–26.
41. S. Kleiner and P.J. Uggowitzer: *Mater. Sci. Eng. A*, 2004, vol. 379, pp. 258–63.
42. D.E. Solas, C.N. Tomé, O. Engler, and H.R. Wenk: *Acta Mater.*, 2001, vol. 49, pp. 3791–801.
43. Y.N. Wang and J.C. Huang: *Mater. Chem. Phys.*, 2003, vol. 81, pp. 11–26.
44. D. Hernández-Escobar, Z.U. Rahman, H. Yilmazer, M. Kawasaki, and C.J. Boehlert: *Philos. Mag.*, 2019, vol. 99, pp. 557–84.
45. S. Suwas and R.K. Ray: *Crystallographic Texture of Materials*, vol. 46, 1st edn., Springer, London, 2014.
46. T.A. Vida, A. Conde, E.S. Freitas, M.A. Arenas, N. Cheung, C. Brito, J. de Damborenea, and A. Garcia: *J. Alloys Compd.*, 2017, vol. 723, pp. 536–47.
47. L. Li, R. Zhang, C. Ban, H. Zhang, T. Liu, H. Zhang, X. Wang, C. Esling, and J. Cui: *Mater. Charact.*, 2019, vol. 151, pp. 191–202.
48. N. Ecob and B. Ralph: *J. Mater. Sci.*, 1983, vol. 18, pp. 2419–29.
49. H. Fan, S. Aubry, A. Arsenlis, and J.A. El-Awady: *Scr. Mater.*, 2016, vol. 112, pp. 50–53.
50. J. Kubásek, D. Vojtěch, E. Jablonská, I. Pospíšilová, J. Lipov, and T. Ruml: *Mater. Sci. Eng. C*, 2016, vol. 58, pp. 24–35.
51. R. Yue, H. Huang, G. Ke, H. Zhang, J. Pei, G. Xue, and G. Yuan: *Mater. Charact.*, 2017, vol. 134, pp. 114–22.
52. T.G. Langdon: *J. Mater. Sci.*, 2009, vol. 44, pp. 5998–6010.

53. T.G. Langdon: *Zeitschrift für Met.*, 2005, vol. 96, pp. 522–31.
54. W. Bednarczyk, J. Kawałko, M. Wątroba, and P. Bała: *Mater. Sci. Eng. A*, 2018, vol. 723, pp. 126–33.
55. M. Demirtas, G. Purcek, H. Yanar, Z.J. Zhang, and Z.F. Zhang: *J. Alloys Compd.*, 2015, vol. 623, pp. 213–18.
56. M. Demirtas, G. Purcek, H. Yanar, Z.J. Zhang, and Z.F. Zhang: *Mater. Sci. Eng. A*, 2015, vol. 644, pp. 17–24.
57. J. Jiang, G. Bi, G. Wang, Q. Jiang, J. Lian, and Z. Jiang: *J. Magnes. Alloy.*, 2014, vol. 2, pp. 116–23.
58. V.A. Krokha: *Strength Mater.*, 1981, vol. 13, pp. 1022–27.
59. J.-H. Shin, J. Jeong, and J.-W. Lee: *Mater. Charact.*, 2015, vol. 99, pp. 230–37.
60. T. Watanabe: *Mater. Sci. Forum*, 1996, vols. 243–245, pp. 21–30.
61. K. Edalati and Z. Horita: *Mater. Sci. Eng. A*, 2011, vol. 528, pp. 7514–23.
62. W. Bednarczyk, J. Kawałko, M. Wątroba, N. Gao, M.J. Starink, P. Bała, and T.G. Langdon: *Mater. Sci. Eng. A*, 2020, vol. 776, p. 139047.
63. T.-S. Cho, H.-J. Lee, B. Ahn, M. Kawasaki, and T.G. Langdon: *Acta Mater.*, 2014, vol. 72, pp. 67–79.
64. E. Mostaed, M.S. Ardakani, M. Sikora-Jasinska, and J.W. Drelich: *Mater. Lett.*, 2019, vol. 244, pp. 203–06.
65. E. Mostaed, M. Sikora-Jasinska, M.S. Ardakani, A. Mostaed, I.M. Reaney, J. Goldman, and J.W. Drelich: *Acta Biomater.*, 2020, vol. 105, pp. 319–35.